SCIENTIFIC REPORTS

OPEN

SUBJECT AREAS:
NANOPARTICLES
NANOPHOTONICS AND PLASMONICS

Received
25 March 2014

Accepted
9 May 2014

Published
28 May 2014

Correspondence and requests for materials should be addressed to H.W.S. (songhw@jlu.edu.cn)

Ag-SiO_2-Er_2O_3 Nanocomposites: Highly Effective Upconversion Luminescence at High Power Excitation and High Temperature

Wen Xu[1], Xiaolei Min[1], Xu Chen[1], Yongsheng Zhu[2], Pingwei Zhou[1], Shaobo Cui[1], Sai Xu[1], Li Tao[1] & Hongwei Song[1]

[1]State Key Laboratory on Integrated Optoelectronics, College of Electronic Science and Engineering, Jilin University, 2699 Qianjin Street, Changchun 130012, China, [2]College of Physics, Jilin University, 2699 Qianjin Street, Changchun 130012, China.

Rare Earth (RE) activated upconversion phosphors (UCPs), have demonstrated significant application potentials in some front fields, including solar energy conversion and bio-application. However, some bottleneck problems should be overcame, such as the lower upconversion efficiency, narrower excitation band, concentration-quenching and temperature-quenching. To solve these problems, the Ag-SiO_2-Er_2O_3 nanocomposites were fabricated, in which the upconversion luminescence (UCL) of Er_2O_3 was white broadband. Through the interaction of Er_2O_3 with surface plasmon (SP) of silver nanoparticles (SNPs), the threshold power for generating broadbands was suppressed largely in contrast to the Er_2O_3 nanoparticles (NPs), while the UCL brightness was enhanced remarkably, ranging from several to 10^4 times, which strongly depended on the power density of excitation light. At excitation power density of 1.50 W/mm^2 of 980 nm light, the UCL intensity of Ag-SiO_2-Er_2O_3 is 40-folds than the well-known $NaYF_4$:Yb^{3+},Er^{3+} commercial powders. And more, it is also interesting to observe that the composites demonstrate two excitation bands extending of 780–980 nm, highly improved UCL with elevated temperature and excitation power density. The UCL mechanism related to UCL enhancement was carefully studied.

UCL, which can convert infrared (IR) radiation into visible light via a two-photon or multi-photon absorption process, has attracted extensive interests because of their potential applications in the field of upconversion lasers, IR quantum counters, three-dimensional (3D) displays, in vivo fluorescence imaging and et al[1–5]. Among various UCP, some RE ions (such as Er^{3+}/Yb^{3+} or Tm^{3+}/Yb^{3+}) co-doped fluoride phosphors are most favorable under 980-nm excitation, because of their sufficient absorption, matching energy levels and low phonon threshold, which lead to relatively efficient UCL[6]. Yet, these UCL have some disadvantages, which can not satisfy the requirement of various practical applications. First of all, their upconversion efficiency is still low, for instance, bulk $NaYF_4$:Yb^{3+}, Er^{3+} in hexagonal phase, which is commonly considered as the most efficient UCP, its efficiency is only 3% under 980-nm excitation. And the strength of corresponding nanosized phosphor ($<$20 nm) is only one of tenth of the bulk[7–8]. Second, because of the presence of the local thermal effect and saturation effect, the UCL intensity will saturate and even quench at relatively high excitation power density, which vitally influences the brightness of UCL[9]. Third, the temperature quenching phenomenon usually happens at high temperature, and the concentration quenching occurs as the concentration of activators is too high[9,10]. In addition, for most of RE activated UCPs based on 4*f*-4*f* transitions, the excitation band is relatively narrow, which is difficult to satisfy the requirement of various optical devices, especially the requirement of solar spectrum conversion[11]. Until now, it is still a challenge to obtain highly efficient UCPs, especially for applications under extreme conditions, such as high power excitation and high temperature.

Recently, Wang et al. observed that some lanthanide oxides micropowders, such as Yb_2O_3, Sm_2O_3, demonstrated efficient UC broadband emissions under the excitation of a 1 W 980-nm laser diode in vacuum, and the upconversion efficiency was estimated to be as high as 10%, and they attributed the broadband emissions to thermal avalanche[12]. Further works were performed to identify the origin of the broadband emissions by Strek et al. and Wang et al[13,14]. Strek attributed the broadband emissions to the charge transfer transition of Yb^{3+}. Our group observed that some lanthanide oxides, such as Er_2O_3, Sm_2O_3, Nd_2O_3 and Pr_2O_3 demonstrated not only

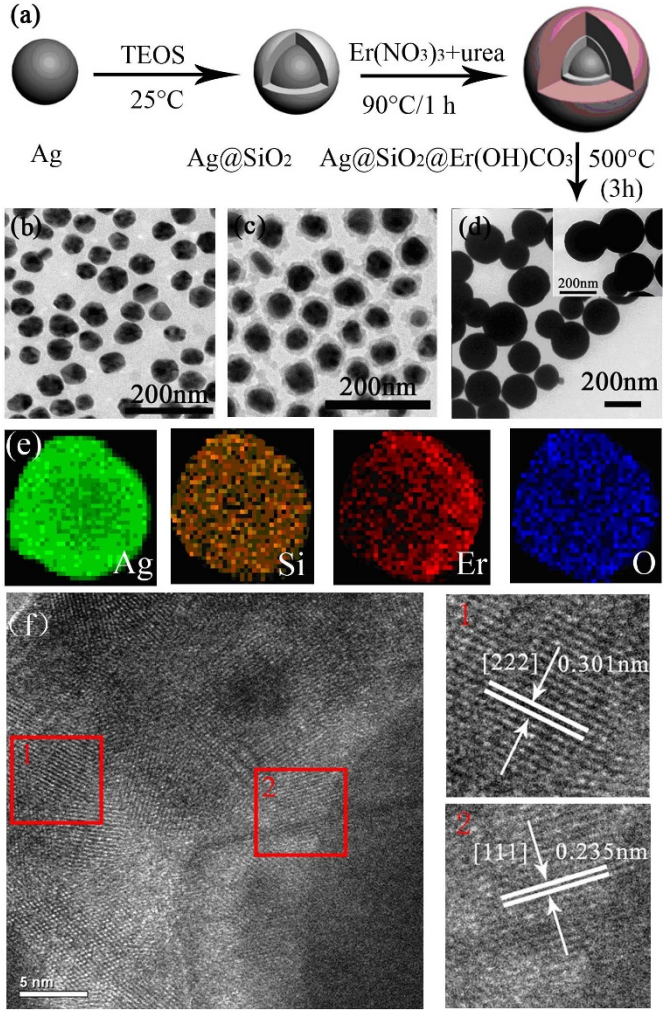

Figure 1 | (a) The specific preparing procedure of Ag-SiO_2-Er_2O_3 nanocomposites, (b-d) TEM images of the as as-prepared Ag NPs, Ag-SiO_2 composites, and Ag-SiO_2-Er_2O_3 nanocomposites, (e) the energy-dispersive X-ray (EDX) mapping of Ag-SiO_2-Er_2O_3 sample at the bottom of the figure, (f) the HR-TEM images of Ag-SiO_2-Er_2O_3 nanocomposites.

sufficient UC broadbands, but also sufficient IR broadbands, ranging of 1000–1700 nm under 980-nm excitation. The evolution of upconversion broadband of micro-sized Er_2O_3 with excitation power were studied, which showed that the broadbands actually came from the contribution of multi-transitions of Er^{3+} ions and spectral broadening of these transitions with elevated temperature[15].

On the other hand, various methods have been explored to improve the strength/efficiency of UCL of nanophosphors[16–19]. Surface enhanced fluorescence of emitters on rough noble metal surfaces is a promised way to largely enhance the UCL of RE doped nanophosphors[20–22]. Recently, UCL enhancement based on the coupling of nanophosphors with noble metals such as gold and silver have been widely observed in UCPs, such as $NaYF_4$:Yb^{3+},Er^{3+} and $NaYF_4$:Yb^{3+},Tm^{3+}. However, no literatures are related to the UCL enhancement of lanthanide oxides, a novel type of efficient UCP. In this paper, the Ag-SiO_2-Er_2O_3 nanocomposites were prepared to obtain effective enhancement of UCL. It is exciting to observe that in the composites, the UCL was improved an order of 10^0–10^4, depending of the excitation power density. And the UCL of Ag-SiO_2-Er_2O_3 composites was more effective than bulk $NaYF_4$:Yb,Er at the high power excitation and the high temperature environment. Furthermore, the UC broadband emission and UCL enhancement mechanism of Ag-SiO_2-Er_2O_3 nanocomposites were proposed.

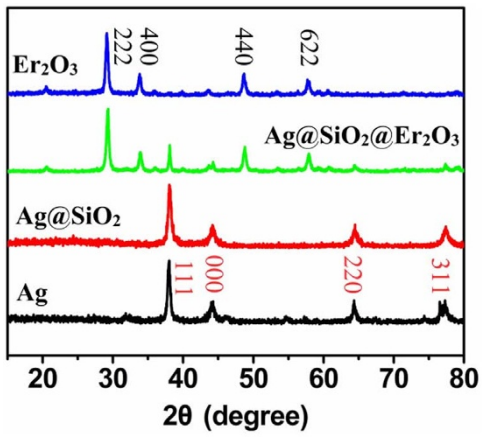

Figure 2 | XRD patterns of the Ag NPs, Ag-SiO_2 composites, Ag-SiO_2-Er_2O_3 composites samples.

Results and Disscussion

Morphology and Structure. First, the morphology of Ag NPs, Ag-SiO_2, Ag-SiO_2-Er_2O_3 nanocomposites and Er_2O_3 NPs were examined by HR-TEM images, as shown in Fig. 1 (b–d). Fig. 1(b) shows the TEM image of the Ag NPs, which indicates that the Ag NPs are basically uniform and monodisperse, with an average diameter of ~60 nm. From Fig. 1(c), it can be distinguished that after coating with SiO_2, Ag-SiO_2 composites with core-shell structure are formed and the composites are monodisperse. The thickness of the SiO_2 shell is about 10–15 nm. In Fig. 1(d), it can be seen that after further coating with Er_2O_3, the sizes of Ag-SiO_2-Er_2O_3 composites grow to 150–200 nm and are sphere-like in shape. Because of large contrast of Er_2O_3, the internal structure of Ag-SiO_2-Er_2O_3 is unable to identify. The illustration of Fig. 1(d) shows the TEM image of Er_2O_3 NPs prepared by the same method, which shows that the diameter of Er_2O_3 NPs is about 150–200 nm, similar to Ag-SiO_2-Er_2O_3 NPs.

In order to further identify the internal structure of the Ag-SiO_2-Er_2O_3 nanocomposites, Fig. 1 (e) shows the EDX mapping to analysis of elements of Ag-SiO_2-Er_2O_3 sample. From left to right, they represent silver, silicon, erbium, and oxygen elements, respectively. It can be seen that all of the elements distribute homogeneously in the whole sphere. Layer gradient distribution of elements can not be identified. This suggests that all the elements have been diffused after annealing at 500°C. In the fringe patterns of the Ag-SiO_2-Er_2O_3 nanocomposites (Fig. 1 (f)), two different fringe spacing was determined to be ~0.301 nm and ~0.231 nm, which corresponded closely with the spacing of the (222) plane of cubic Er_2O_3 (0.307 nm) (JCPDS No. 77-0464) and the (111) plane of fcc silver (0.235 nm) (JCPDS No. 87-0717), respectively. From the HR-TEM, we can further deduce the forming of Ag-SiO_2-Er_2O_3 nanocomposites.

Fig. 2 shows the XRD patterns of the samples Ag NPs, Ag-SiO_2 composites, Ag-SiO_2-Er_2O_3 nanocomposites. Comparing to the corresponding standard cards, it can be seen that silver and Er_2O_3 NPs in pure cubic phase are formed. And, after coating with SiO_2 shells, no extra patterns could be identified except Ag NPs, because SiO_2 shells are amorphous in phase. In the Ag-SiO_2-Er_2O_3 composites, both XRD patterns of cubic silver and cubic Er_2O_3 could be identified, as shown in the figure, implying the formation of Ag-SiO_2-Er_2O_3 composites.

Fig. 3 shows the UV-Vis-Infrared absorption spectra of Ag NPs, Ag-SiO_2 composites and Ag-SiO_2-Er_2O_3 composites. It can be seen that the silver NPs demonstrate relatively narrow surface plasmon absorption (SPA), peaking around 420 nm. After coating with SiO_2 shell, the SPA of silver shifts toward red side due to the dielectric effect[23,25]. It's interesting to observe that the SPA of Ag-SiO_2-Er_2O_3 composites demonstrates broadbands, extending from 350–1100 nm.

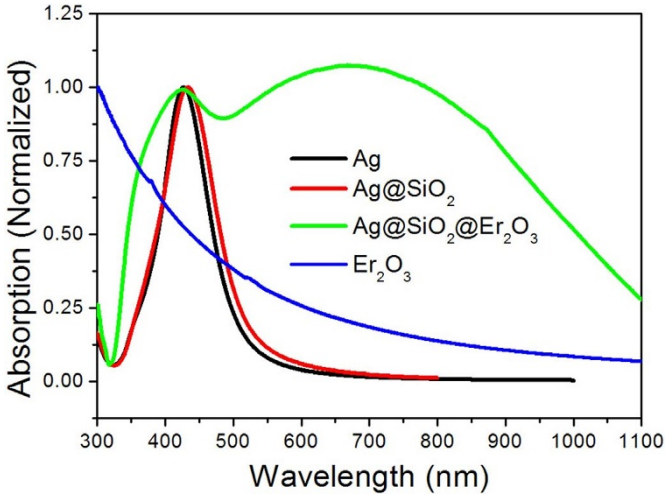

Figure 3 | The absorption spectra of Ag NPs, Ag -SiO_2composites and the Ag-SiO_2-Er_2O_3 composites.

Two bands can be identified, one locates around 450 nm, and the other locates around 700 nm, corresponding to the transverse and longitude SPA of silver, respectively. Furthermore, as a comparison, the absorption spectrum of Er_2O_3 NPs was given in Fig. 3, it can be seen that there is no obvious peak, and with the decrease of wavelength the absorption increases, attributed to the scattering of the Er_2O_3 NPs. This suggests that, in the Ag-SiO_2-Er_2O_3 composites, the silver NPs might have been changed into small NPs and these small NPs demonstrate anisotropic, leading to the occurrence of longitude SPA of silver.

UCL Enhancement of Ag-SiO_2-Er_2O_3 Nanocomposites. Fig. 4 (a) and Fig. 4 (b) show the UCL spectra of Er_2O_3 NPs and Ag-SiO_2-Er_2O_3 composites under the excitation of 0.26–1.41 W/mm^2 980 nm light, respectively. It can be seen that, with relatively low excitation power, the emission spectra of Er_2O_3 and Ag-SiO_2-Er_2O_3 both have two groups of emission lines. The lines in the green range correspond to the $^2H_{11/2}/^4S_{3/2}$-$^4I_{9/2}$ transitions, while those in the red range to the $^4F_{9/2}$-$^4I_{15/2}$ transitions, and the red emissions of $^4F_{9/2}$-$^4I_{15/2}$ are dominant for Er_2O_3 NPs. This is in consistent with the result of micro-sized Er_2O_3 and can be mainly attributed to the contribution of cross relaxation channels for Er^{3+} ions[15]. And with increasing the excitation power, a broadband emission ranging of 400–800 nm appears and the intensity ratio of the red to the green emission also decreases with the increasing excitation power. In addition, under the excitation of relatively high excitation power, both Er_2O_3 and Ag-SiO_2-Er_2O_3 NPs demonstrate broadband emissions, and their central positions both locate around 600 nm (~2 eV), independent of excitation power density. It should be highlighted that in contrast to Er_2O_3, the threshold power of generating white broadbands in the Ag-SiO_2-Er_2O_3 nanocomposites degraded from 0.65 W/mm^2 to 0.26 W/mm^2. In our previous work, the UCL of Er_2O_3 microsized powders was studied, which demonstrated considerable difference comparing to the present Er_2O_3 NPs and Ag-SiO_2-Er_2O_3 composites. As a comparison, the UCL spectra of bulk Er_2O_3 were shown in Fig. 4(c)[15]. In the bulk

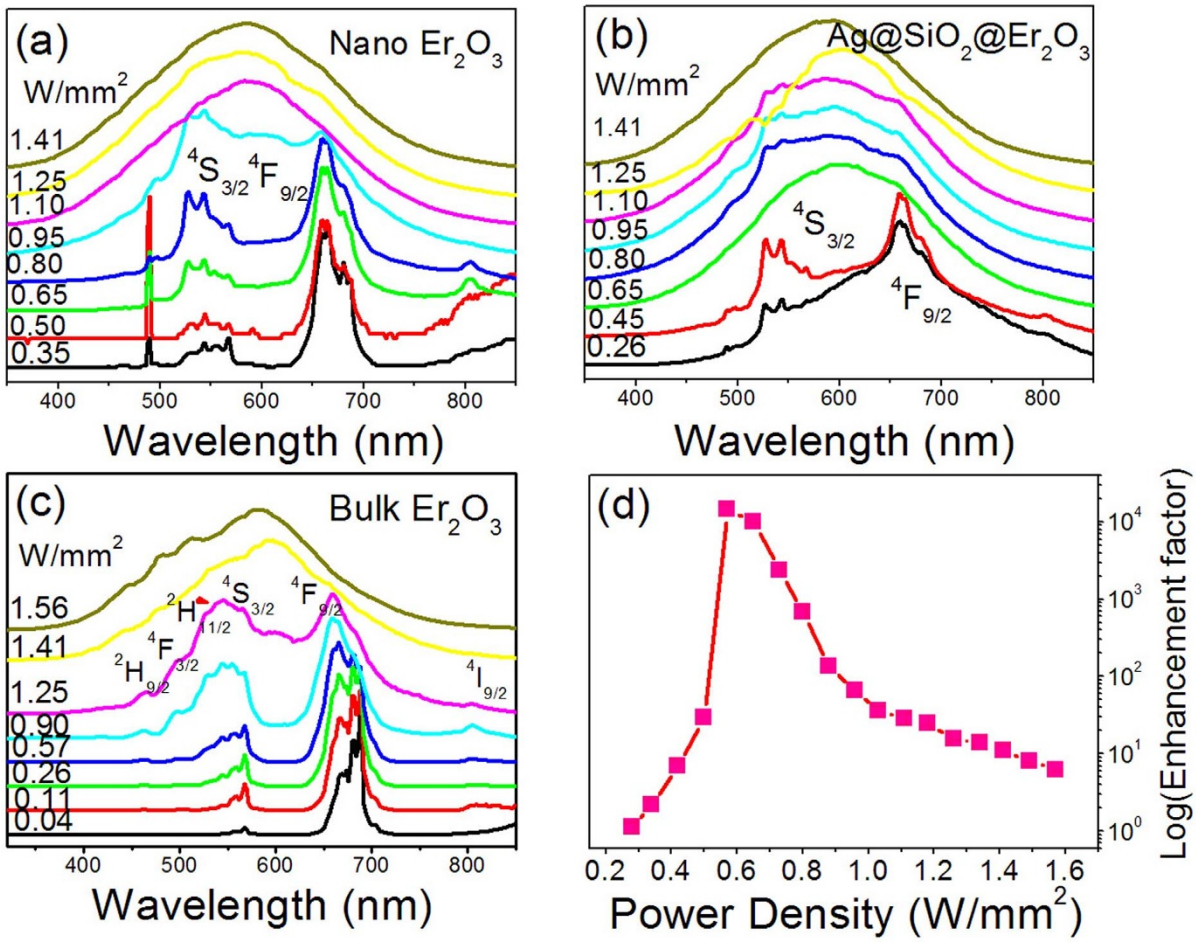

Figure 4 | (a–c) The UCL spectra of Er_2O_3 NPs, Ag-SiO_2-Er_2O_3 composites, and the UCL spectra of bulk Er_2O_3 under as a function of 980 nm excitation power density, respectively, (d) the UCL EF as a function of excitation power density.

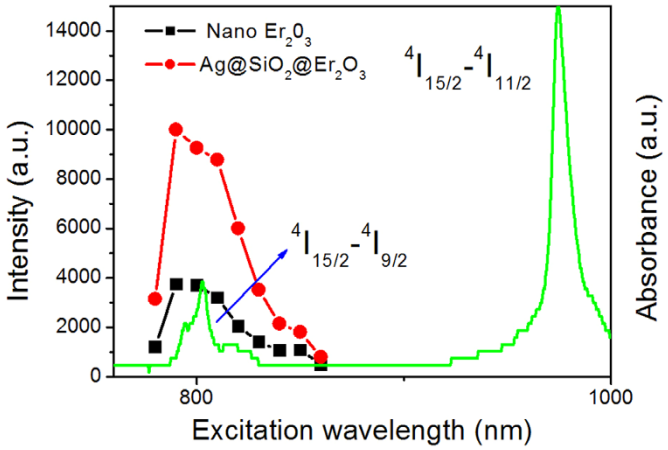

Figure 5 | The UC excitation spectra in a range 780-860 nm in Er_2O_3 NPs and Ag-SiO_2-Er_2O_3 nanocomposites, and the absorption spectra of Er^{3+} ions.

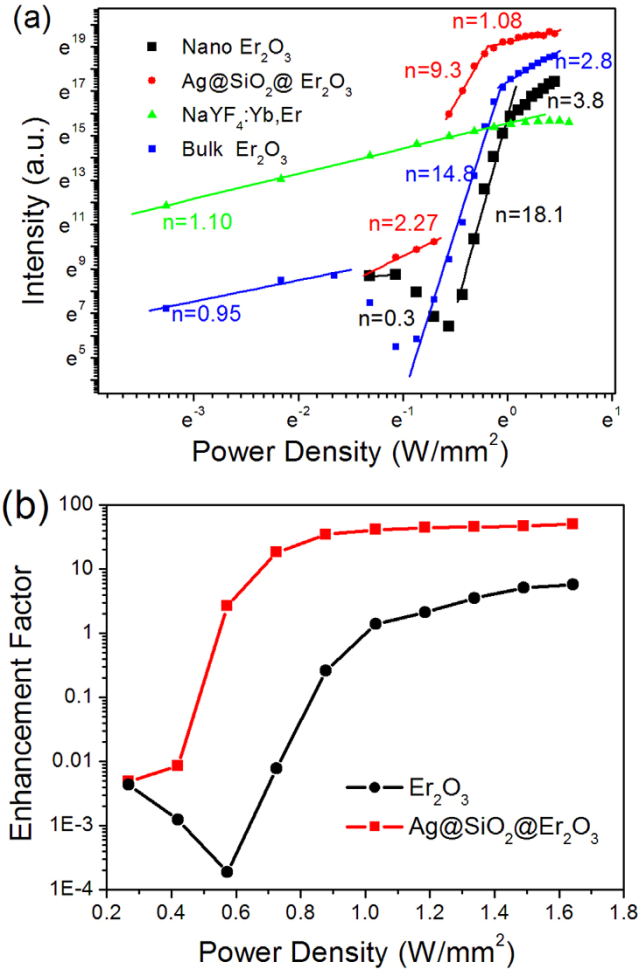

Figure 6 | (a) The power density dependence of integral UCL intensity of Er_2O_3 NPs, Ag-SiO_2-Er_2O_3 composites, bulk $NaYF_4$:Yb,Er, and bulk Er_2O_3 under 980 nm excitation; (b) the UCL EF as a function of excitation power density.

Er_2O_3, the UCL of Er^{3+} ions originates from the emissions of Er^{3+} all the time. The generation of broadbands originates from the contribution of different transitions of Er^{3+} ions, $^2H_{9/2}/^4F_{3/2}$-$^4I_{15/2}$ (three-photons), $^2H_{11/2}/^4S_{3/2}$-$^4I_{15/2}$ (two-photon) and $^4F_{9/2}$-$^4I_{15/2}$ (three-photon) and their spectral broadening. In the Er_2O_3 NPs and Ag-SiO_2-Er_2O_3 composites, the broadband locates around 600 nm and is independent of excitation power, which is very similar to our previous result observed in YVO_4: Yb^{3+}, Er^{3+} NPs[26]. It could be attributed to the UCL of oxygen defects. Actually, the broadband UC emissions in lanthanide oxides are quite complex and their origins have not been clarified, and basically, they could be attributed to charge transfer transitions of rare earths, defect transitions, or electron-hole pairs[13,27,28]. The mechanism will be discussed later in details.

Fig. 4(d) shows the UCL enhancement factor (EF, which is defined as the ratio of UCL intensity of the Ag-SiO_2-Er_2O_3 composites to that of Er_2O_3 NPs) as a function of excitation power density. It is interesting to see that the enhancement factor (EF) varies significantly with excitation power density, from several times to 10^4 times. At relative low excitation power, the UCL intensity of Ag-SiO_2-Er_2O_3 increases from several times to several ten times over that of Er_2O_3. As the excitation power increases to 0.57 W/mm^2, due to the sudden change of UCL (see Fig. 6), the enhancement factor dramatically increases to 9850 times, which shows that the UCL intensity of Ag-SiO_2-Er_2O_3 is about four orders higher than that of Er_2O_3. As the excitation power density increases further, EF gradually decreases. And at relatively high excitation power density (0.8–1.6 W/mm^2), EF gradually decreases to 7 times.

It is interesting to observe that, in the Er_2O_3 NPs, the UCL of the broadband was obtained not only under the excitation of 980 nm, corresponding to the excitation of $^4I_{15/2}$-$^4I_{11/2}$ transition of Er^{3+} ions, but also under the excitation of 780–860 nm laser, corresponding to the excitation of $^4I_{15/2}$-$^4I_{9/2}$ transition of Er^{3+} ions, as shown in Fig. 5. The UCL spectra of Ag-SiO_2-Er_2O_3 under the excitation of 808 nm light were recorded in Fig. S1, which showed that the UC emission bands extended of 400–750 nm, and the central emissions located at around 660 nm, corresponding to the $^4F_{9/2}$-$^4I_{15/2}$ transitions of Er^{3+} ions and the other transitions of Er^{3+} ions, $^2H_{11/2}/^4S_{3/2}$ -$^4I_{15/2}$ and $^2H_{9/2}/^4F_{3/2}/^4F_{7/2}$-$^4I_{15/2}$ could also be identified. From the absorption spectra of Er^{3+} ions in Fig. 5, it's known that the absorption value of 808 nm is significantly lower than 980 nm, the achievement of UC broad band emission under 808 nm excitation should have higher excitation power density than that under 980 nm excitation. And the excitation power density of 808 excitation (0.29–0.37 W/mm^2) in Fig S1 is lower than that with the 980 nm excitation, leading to the weaker UC broad band emission. Because the intrinsic transition of Er^{3+} ($^4F_{9/2}$-$^4I_{15/2}$) is the main emission, leads to red-shift of the central emissions to 660 nm, so the broad band for 808 nm excitation is different from that for 980 nm excitation. In fact, we measured the UC broad band emission under 808 nm excitation (with excitation power density ~6 W/mm^2, at the excitation spectra measurement), the broad band emission is exactly in accordance with those under 980 nm excitation. Furthermore, the UC excitation spectra in the range of 780–860 nm in Er_2O_3 NPs and Ag-SiO_2-Er_2O_3 nanocomposites were measured and compared (the excitation power density is ~6 W/mm^2), as shown in Fig. 5. It should be noted that the UC broadband emission spectra are exactly in accordance with those under 980 nm excitation. With the excitation range of 780–860 nm, the obvious excitation bands were identified, centering around 790 nm, for both Er_2O_3 NPs and Ag-SiO_2-Er_2O_3 nanocomposites, which were in accordance with the $^4I_{15/2}$-$^4I_{9/2}$ excitation transition of Er^{3+} ions. In Ag-SiO_2-Er_2O_3 nanocomposites, the UCL enhancement of several times was observed in the whole range from 780 nm to 860 nm. The UCL enhancement in Ag-SiO_2-Er_2O_3 nanocomposites could be due to three reasons: First, under 780–980 nm excitation, corresponding to the longitude SPA of Ag NPs, ET from Ag NPs to Er_2O_3 happened effectively, leading to UCL enhancement of Ag-SiO_2-Er_2O_3 nanocomposites; Second, the excitation and emission strength enhanced due to the field enhancement effect; Third, the thermal effect happened with the surface plasmon excitation of Ag NPs, leading to the thermal avalanche

happening easily, and to the decrease of excitation threshold of the broadband emission.

In order to further confirm the mechanism of UCL enhancement, the Ag-SiO_2-Y_2O_3:10%Yb,1%Er nanocomposites as well as Y_2O_3:10%Yb, 1%Er were also investigated for comparison and the intrinsic transitions coming from Er^{3+} and the broadband were indentified. The intrinsic transition of Er^{3+} ions was much higher than that of Er_2O_3 because of concentration quenching[10] and broadband emission was significantly lower than that of Er_2O_3. In comparison to Y_2O_3:Yb^{3+},Er^{3+}, the emission of Er^{3+} in Ag-SiO_2-Y_2O_3:Yb, Er was suppressed, while the broadband emission was improved. This suggests that the UCL enhancement of the broadband emission mainly originates from the thermal effect, instead of ET from Ag to Er_2O_3 or field enhancement effect (see Fig. S2).

Ag-SiO_2-Er_2O_3 Composites: Strong UCL at High Power Excitation and at High Temperature. Fig. 6 (a) shows the power density dependence of integral UCL intensity of Er_2O_3 NPs and Ag-SiO_2-Er_2O_3 nanocomposites on excitation power density of 980 nm light in logarithmic coordinate. It can be seen that basically the power density dependence can be divided into three periods. For Er_2O_3 NPs, the overall UCL intensity first decreases slowly with the increasing excitation power before the generation of UC broadband. As the UC broadband appears, the UCL intensity increases dramatically with the increasing excitation power, with a power law of $I \sim P^n$ and the slope n is as high as 18.1. Then, as the excitation power continuously increases, the slope n drops to 3.8. For the Ag-SiO_2-Er_2O_3 composites, the UCL intensity increases with a slope of $n = 2.27$ before generation of the broadband. Then, a sudden increase occurs, accompanying the generation of UC broadband, and after that, the UCL intensity increases with a slope of $n = 9.3$. Finally, the slope drops to $n = 1.07$. Presently, the super-strong and complex power dependence of the UCL intensity has not been completely understood. It is suggested that during the UC process, photon avalanche or thermal avalanche probably happens[12]. For comparison, the excitation power density dependence of integral UCL intensity (including $^2H_{11/2}$, $^4S_{3/2}$, $^4F_{9/2}$-$^4I_{15/2}$ transitions) of the bulk $NaYF_4$:Yb,Er were given in Fig. 6. The value of slope n was about 1.1, which was much smaller than the required photon number (n = 2, 3) populating to the corresponding levels. This can be attributed to the saturation effect as well as the local thermal effect induced by the laser exposure. And with further increasing the excitation power, the UCL intensity has a decrease in $NaYF_4$:Yb,Er. Fig. 6(b) shows the UCL enhancement factor (EF1, which is defined as the ratio of UCL intensity of Er_2O_3 and Ag-SiO_2-Er_2O_3 NPs to that of the $NaYF_4$:Yb,Er powders. respectively) as a function of excitation power density. From Fig. 6(b), it's observed that at lower excitation power density, the traditional UCL material such as $NaYF_4$:Yb,Er has great advantage because of the lower excitation threshold, however under higher power excitation, Er_2O_3 and Ag-SiO_2-Er_2O_3 nanocomposites has higher UCL intensity, because of the high saturation effect and the local thermal effect in $NaYF_4$:Yb^{3+}, Er^{3+}. It's worth noting that as the excitation power approached to 1.5 W/mm^2, the UCL strength of Ag-SiO_2-Er_2O_3 nanocomposites was 45 times over $NaYF_4$:Yb^{3+}, Er^{3+} powders.

As is known, the concentration quenching phenomenon would happen especially in UCL material as the concentration of activators is too high because of cross relaxation, which limits the UCL strength of the RE activated UCP[10]. Recently, Jin et al. reported that high excitation irradiance could alleviate concentration quenching in UCL when combined with high activator concentration[29]. In Er_2O_3 and Ag-SiO_2 -Er_2O_3 NPs, which the concentration of activator was is 100% in molar ratio, the similar phenomenon was also observed. As the excitation power density was lower, the concentration quenching happened seriously, which was confirmed by the much lower UCL intensity of Er_2O_3 in comparison to that of Y_2O_3:Yb,Er. However, at sufficient excitation power, the effective UCL was generated for both nanosized and bulk Er_2O_3 (See Fig. 6), and Ag-SiO_2 -Er_2O_3, implying the concentration quenching was perfectly suppressed (In the bulk Er_2O_3, the luminescent centers were contributed by Er^{3+} ions all the time, and in the nanosized samples, the generation of broadband originated from the excitation of Er^{3+} ions).

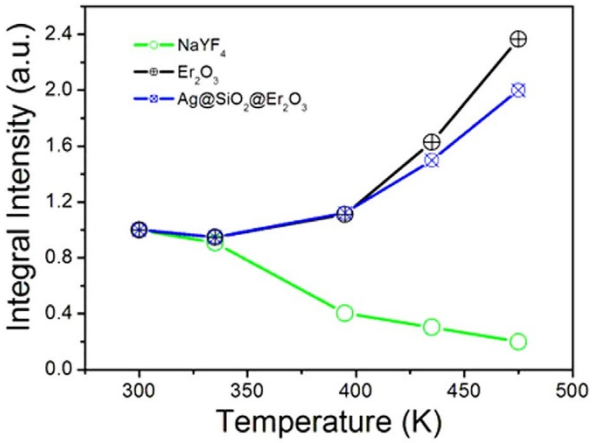

Figure 7 | The temperature dependence of the UCL integral intensity (normalized at 300 K) of Er_2O_3 NPs, Ag-SiO_2-Er_2O_3 composites, and bulk $NaYF_4$:Yb, Er on 980 nm light excitation.

Furthermore, the temperature dependence of the UCL integral intensity (normalized at 300 K) under 1.10 W/mm^2 980 nm excitation were recorded for nanosized Er_2O_3, Ag-SiO_2 -Er_2O_3, and bulk $NaYF_4$:Yb, Er in the range of 300–475 K, as shown in Fig. 7. It's exciting to observe that the integral intensity increases 2.4 fold and 2.0 fold for Er_2O_3 and Ag-SiO_2-Er_2O_3, respectively, while reduces to the 20% of original for $NaYF_4$:Yb,Er as the temperature increases from 300 K to 475 K, implying significant temperature quenching. For Er_2O_3 and Ag-SiO_2-Er_2O_3 composite, the high temperature promotes the photon avalanche, leading to the increase of the UC broad emission with the increasing temperature. From the results, we can deduce that it's difficult to realize effective UCL in traditional materials (such as $NaYF_4$:Yb,Er,) at high power excitation, high concentration activator and high temperature conditions. While for Ag-SiO_2 -Er_2O_3 composite, it overcomes these problems, which has great significance in extreme conditions.

The origin of UC Broadband Emission. In order to better understand the origin of the UCL process, the temperature and photocurrent, as a function of excitation power density in the Er_2O_3 NPs and Ag-SiO_2-Er_2O_3 nanocomposites samples under 980 nm excitation, were recorded in Fig. 8. The temperature measurement under the exposure of 980 nm light was achieved by burying the thermocouple thermometer into the powder plate samples. In Fig. 8(a), it can be seen that, in Er_2O_3 NPs and Ag-SiO_2-Er_2O_3 nanocomposites, the temperature varies from 375 K to 600 K, 470 K to 680 K under the excitation power ranging from 0.25 W/mm^2 to 1.5 W/mm^2, respectively. And Ag-SiO_2-Er_2O_3 nanocomposites have higher temperature than that of Er_2O_3. And the temperature of broadband emission happening is about 460 K for the two samples. The irradiation power density corresponding to 460 K for the Ag-SiO_2-Er_2O_3 nanocomposites is lower than that for the Er_2O_3 sample (the necessary temperature for generating holes in the valence band). This indicates that the occurrence of broadband UCL is accompanied by the generation of thermal holes in valence band. And such the high temperature generates thermal holes in the valence band. It should be noted that the temperature is much lower than the necessary temperature for generating sufficient blackbody radiation (~2500 K)[30]. The power density dependence of the photocurrent of Er_2O_3 NPs and Ag-SiO_2-Er_2O_3 nanocomposites

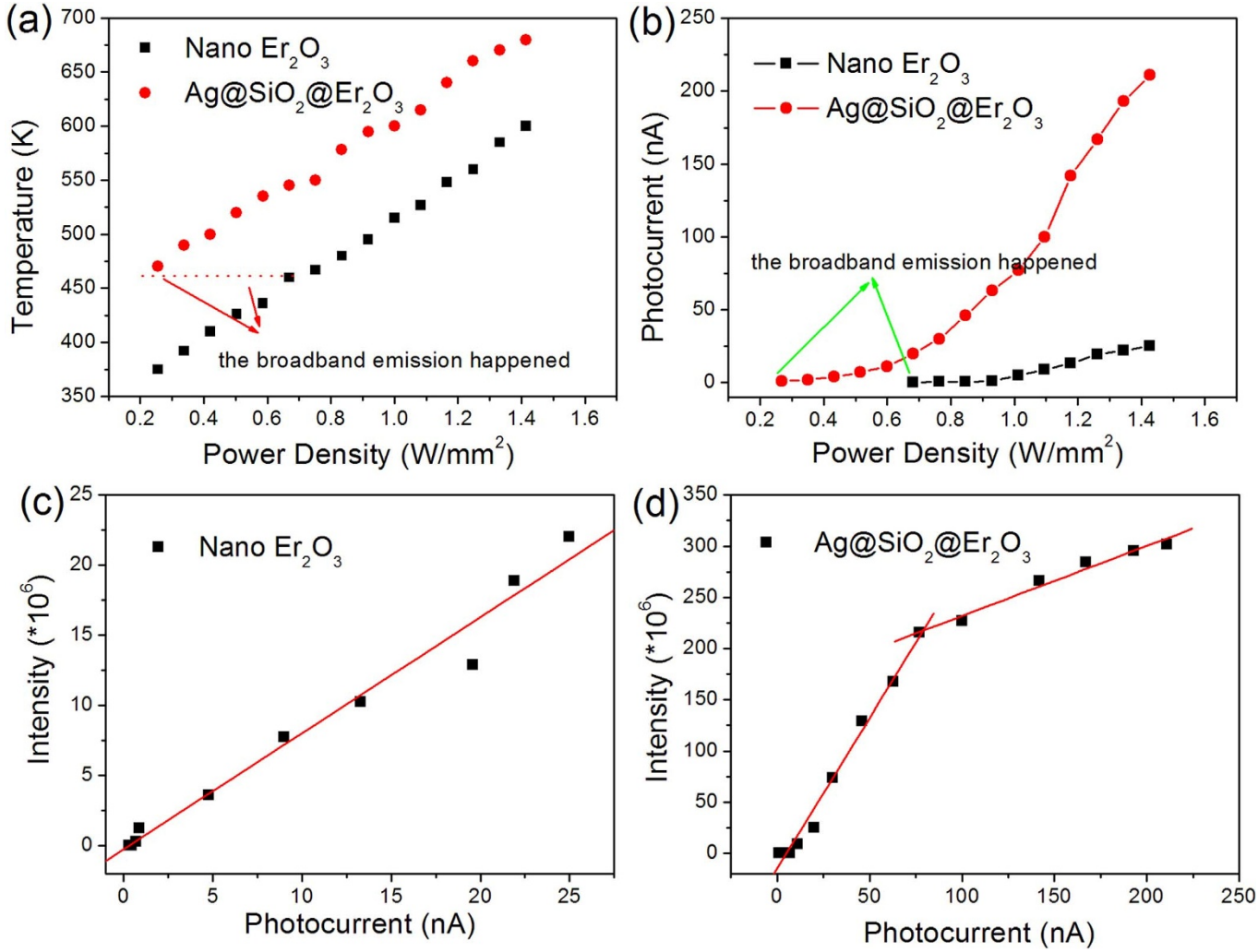

Figure 8 | The temperature (a) and photocurrent (b) as a function of excitation power density in the Er_2O_3 and Ag-SiO_2-Er_2O_3 nanocomposites samples under 980 nm excitation, the UCL intensity of Er_2O_3 (c) and Ag-SiO_2-Er_2O_3 composites (d) as a function of the photocurrent.

was shown in Fig. 8b. The photocurrent increases with the excitation power density, which is along with generating the UC broadband. And the photocurrent has higher value in Ag-SiO_2-Er_2O_3 nanocomposites. It's interesting to observe that the integral intensity of UC broadband in Er_2O_3 and Ag-SiO_2-Er_2O_3 nanocomposites satisfies with the linear dependencies with the photocurrent increasing (Fig. 8c–d). From Fig. S3, the photocurrent increases dramatically with the increasing excitation power, with a power law of Ic ~ P^n and the slope n is 6.9 and 3.8 in Er_2O_3 and Ag-SiO_2-Er_2O_3 nanocomposites, respectively. The high slope n of UC borad band (I ~ P^n) would be attributed to the high slope n of photocurrent (Ic ~ P^n). Furthermore, the temperature dependent photocurrent of Er_2O_3 and Ag-SiO_2-Er_2O_3 composites was shown in Fig. 9. According to the Boltzmann distribution, the relationship between the electrical conductivity σ and the temperature T can be written as, $\sigma = \sigma_0 e^{-\frac{\Delta E}{k_0 T}}$, where k_0 is Boltzmann's constant, ΔE is the energy difference between the valence band maximum of Er_2O_3 and the unknown confined state in the bandgap (Most of RE_2O_3 compounds were p-type semiconductors.[31]). According to Figure Fig. 9, ΔE was deduced to be 1.11 eV and 1.21 eV. As to the origin of the unknown state, has not been clarified. Here, we suggest that the excited state of Er^{3+} ($^4I_{13/2}$) is the possible candidate of the confined state (its ground state locates above the valance band maximum).

Recently, Strek et al. have also observed UC broadband in $LiYbP_4O_{12}$ and its origin was attributed to the radiative charge transfer transitions of Yb^{3+} or Yb^{2+})[13].According to the literatures, the charge transfer (CT) emissions of Yb^{2+} and Yb^{3+} located at around 560 nm (~2.2 eV) and 650 nm (~1.9 eV) in oxide compounds, respectively, which was different from the present result at 600 nm (~2.0 eV). In our previous work, in YVO_4:Yb, Ln^{3+} (Er^{3+}, Tm^{3+},

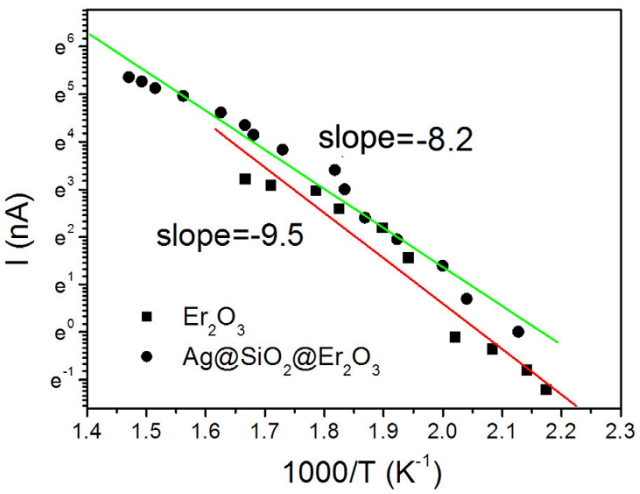

Figure 9 | The plot of natural logarithm of the photocurrent (I) against the reciprocal of absolute temperature in Er_2O_3 and Ag-SiO_2-Er_2O_3 composites under the excitation of 980 nm light.

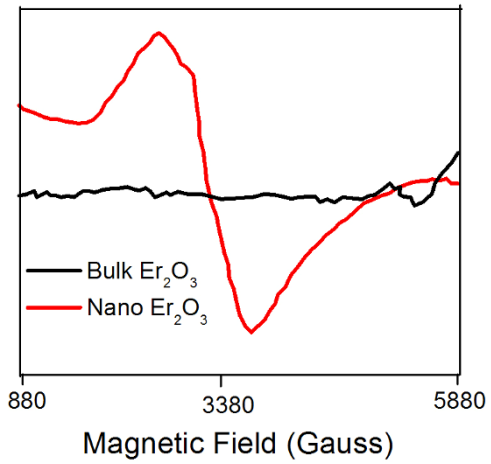

Figure 10 | The EPR spectra for bulk Er_2O_3 and Er_2O_3 NPs at room temperature.

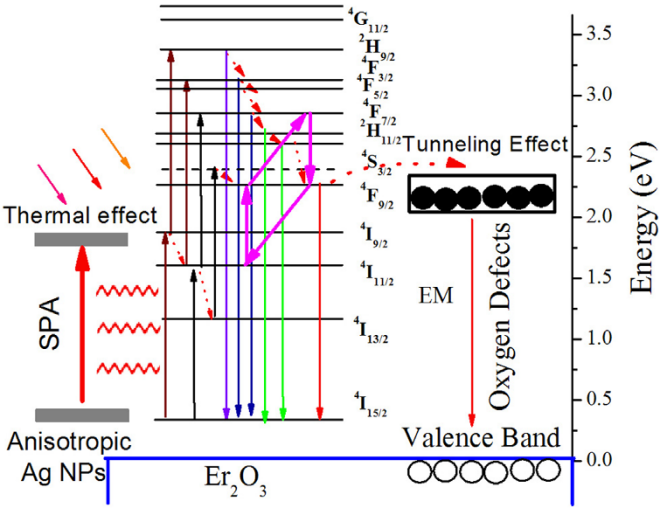

Figure 11 | The schematic of the possible mechanism of UC broadband emission in Er_2O_3 NPs and UCL enhancement in Ag-SiO_2-Er_2O_3 nanocomposites.

Ho^{3+}), the UC broadband located at 600 nm (~2.0 eV) was also observed, which is exactly the same as this work[26]. The origin of the UC broadband was attributed to the defect emissions related to oxygen defects. Fig. 10 shows the EPR spectra of bulk Er_2O_3 and Er_2O_3 NPs at the room temperature. The microwave frequencies and power are 9.438 GHz and 1 mW, respectively. It can be seen that in bulk Er_2O_3, the EPR signal was not observed, while in Er_2O_3 NPs, a EPR signal was detected in the range of 880–5580 Gauss with g factor about 1.9951. In general, when the actual measured g factor is lower than the free electron g factor (g_{free} = 2.0023), the EPR signal represents the electron trap[32]. In other words, the EPR signal in Er_2O_3 NPs is assigned to the oxygen defects. It's known that the bulk material has perfect lattice and little defects, so the EPR signal is not detected in bulk Er_2O_3. These results further prove that the UC broadband originates from the oxygen defects emission in Er_2O_3 NPs, and it's completely different from the UC broadband in bulk Er_2O_3 reported previously[15].

Based on the above discussions, it is suggested that for the Er_2O_3 NPs and Ag-SiO_2-Er_2O_3 nanocomposites samples, the efficient absorption of NIR photons, improved temperature, and oxygen defects are the key important factors for the generation of high-intensity UC broadband. Fig. 11 shows the schematic of the possible mechanism of UC broadband emission in Er_2O_3 NPs and UCL enhancement in Ag-SiO_2-Er_2O_3 nanocomposites. In Er_2O_3, Er^{3+} ions on ground states $^4I_{15/2}$ are mainly excited to $^4I_{11/2}$ and $^4I_{9/2}$ by the first-step ET from excited Er^{3+} under 980 nm and 780–860 nm excitation, through the subsequent nonradiative relaxation of $^4I_{11/2}$, $^4I_{9/2}$, the electrons populate to the $^4I_{13/2}$, $^4I_{9/2}$ levels, respectively, and then are excited to $^4F_{7/2}$ and $^2H_{9/2}$, or $^4F_{9/2}$ and $^4F_{5/2}$ by the second-step ET or excited-state absorption. At the low excitation power, the electrons stepwise populate to the $^2H_{9/2}$, $^4F_{5/2}$, $^4F_{5/2}$, $^2H_{11/2}$, $^4S_{3/2}$, and $^4F_{9/2}$, subsequently generating the blue, green and red emissions[33–35]. As the excitation power is high enough, the temperature of Er_2O_3 or Ag-SiO_2-Er_2O_3 samples increases considerably, leading to the cross relaxation ($^4F_{7/2}$ + $^4I_{11/2}$ → $^4F_{9/2}$ + $^4F_{9/2}$) exacerbating. Because the multi-photon (n > 3) UCL was not observed in Er_2O_3 or Ag-SiO_2-Er_2O_3 samples, it's confirmed that most of the electrons on $^4F_{9/2}$ are captured by the oxygen vacancy states through the tunneling effect. Meanwhile, on the valence band of Er_2O_3 or Ag-SiO_2-Er_2O_3 samples, a large number of holes were generated, which could be confirmed by the occurrence of photocurrent (see Fig. 9). It is suggested that the electrons on oxygen vacancy states recombined with holes in the valence band of Er_2O_3, generating broadband UCL. (The location of the oxygen vacancy states was confirmed by the UC broadband emission.) It should be pointed out that the radiative transition rate of electron-hole recombination of semiconductor was at least several orders larger than the 4*f*-4*f* transitions of Er^{3+} ions[36,37], and thus could exceed the nonradiative relaxation rate of Er^{3+} ions, preventing the thermal quenching of UCL. On the contrary, due to the direct 4*f*-4*f* radiative transition rate of excited Er^{3+} ions was much smaller than the nonradiative relaxation rate at elevated temperature, this kind of UCL was unavoidably quenched. And in Ag-SiO_2-Er_2O_3 nanocomposites, the improvement of UCL are mainly attributed to the thermal effect with the SP excitation of Ag NPs, which is beneficial to generating thermal holes in the valence band, resulting in the decrease of threshold power for generating white light.

Conclusions

In this paper, Ag-SiO_2-Er_2O_3 nanocomposites were prepared by a wet-chemical method and characterized by XRD patterns, TEM images, EDX mapping, and UV-vis absorption spectra. The results show that the anisotropic small Ag NPs distribute randomly and have strong SPA in the range of 400–1000 nm in the composites. In the composites the UCL intensity was improved greatly over that of Er_2O_3, depending strongly on excitation power of 980-nm laser diode. The enhancement factor changed from several times until to ~10^4, and under the excitation of 1.5 W/mm^2, the UCL intensity of Ag-SiO_2-Er_2O_3 improved 40 times over the well known $NaYF_4$:Yb^{3+},Er^{3+} commercial powders. And more, it should be noted that the UCL of the broadband in Ag-SiO_2-Er_2O_3 as well as Er_2O_3 demonstrated favorable two excitation bands, could effectively avoid concentration quenching and temperature quenching. The mechanism of the broadband UCL in Er_2O_3 and Ag-SiO_2-$Er_2O_3$was attributed to the electron-hole combination and the UCL enhancement in Ag-SiO_2-Er_2O_3 was mainly attributed to thermal effect, which dramatically increased the density of holes on the valence band. Overall, the Ag-SiO_2-Er_2O_3 composite is a novel favorable UCP with super intense UCL and is promised to work at extreme conditions such as at high pumping power and at high temperature.

Methods

Sample preparation. The specific preparing procedure was as follows, shown in Fig. 1(a). Firstly, the 60-nm silver was prepared through ethylene glycol reduction method[8]. In a typical synthesis process, 3.3 g PVP-K40 was first dissolved in EG at the room temperature, after that 0.14 g $AgNO_3$ was added and stirred for ten minutes. The mixture was heated to 120°C for an hour, then allowed to cool naturally. The whole process had the protection of nitrogen. The Ag nanoparticles (NPs) were isolated by centrifugation and washed several times with acetone and deionized water. Then, Ag-SiO_2 composites were prepared by the modified STÖBER method[23]. The

as-prepared Ag NPs and a small amount of ammonia and TEOS were dissolved in ethanol and stirred for 24 hours at room temperature. Then, the precipitates were collected and washed three times with alcohol. After that, the precipitates (Ag-SiO_2) were dissolved in deionized water, added into Er $(NO_3)_3 \cdot H_2O$ and urea, heated at 90°C for an hour and cleaned with alcohol three times. Then, the obtained sample was annealed at 500°C for 3 hours[24]. At last, the Ag-SiO_2-Er_2O_3 composites were collected. For comparison, Er_2O_3 NPs were synthesized by a similar method.

Characterization. The morphology of the products was recorded on a Hitachi H-8100IV transmission electron microscope (TEM) under an acceleration voltage of 200 kV. The energy-dispersive X-ray (EDX) elemental mapping images were recorded on a FEI Tecnai G2 S-Twin microscope under a working voltage of 200 kV equipped with EDX spectrometer. The phase structure and purity of the as-prepared samples were characterized by X-ray power diffraction (XRD) with a Rigaku D/max 2550 X-ray diffractometer, using a monochromatized Cu target radiation resource (λ = 1.54Å). UV/Vis–NIR absorption spectra were measured with a Shimadzu UV-1800PC UV/Vis–NIR scanning spectrophotometer in the range from 300 to 1100 nm. In the measurements of power-dependent UCL spectra, a continuous 980 nm was used to pump the samples. A visible photomultiplier (350–850 nm) combined with a double-grating monochromator were used for spectral collection. In order to obtain the excitation spectra of UCL, the integrated intensity over the 350–720 nm range of the emission was plotted versus excitation wavelength, and that process was fulfilled by using a Titanium: Sapphire oscillator (Mira-HP; Coherent, Santa Clara, CA) which worked in the CW mode which was pumped by a continuous wave laser (Verdi-V18; Coherent). The photo current-voltage (I–V) curves were acquired by a source-measurement unit under the illumination of continuous 980 nm diode laser or Titanium: Sapphire oscillator which worked in the CW mode (790 ~ 830 nm). Electron paramagnetic resonance (EPR) spectra were measured by the JESFE3AX electron spin resonance spectrophotometer at room temperature.

1. Auzel, F. Upconversion and Anti-Stokes Processes with f and d Ions in Solids. *Chem. Rev.* **104**, 139 (2004).
2. Esterowitz, L., Noonan, J. & Bahler, J. Enhancement in a Ho^{3+}–Yb^{3+} quantum counter by energy transfer. *Appl. Phys. Lett.* **10**, 126–127 (1967).
3. Rapaport, A., Milliez, J., Bass, M., Fellow, L. & Cassanho, A. Review of the Properties of Up-Conversion Phosphors for New Emissive Displays. *J. Disp. Technol.* **2**, 68–78 (2006).
4. Yu, X. F. *et al*. Dopant-Controlled Synthesis of Water-Soluble Hexagonal $NaYF_4$ Nanorods with Efficient Upconversion Fluorescence for Multicolor Bioimaging. *Nano Res.* **3**, 51–60 (2010).
5. Wang, L. Y. *et al*. Fluorescence Resonant Energy Transfer Biosensor Based on Upconversion-Luminescent Nanoparticles. *Angew. Chem. Int. Edit.* **44**, 6054–6057 (2005).
6. Wang, F. & Liu, X. G. Recent Advances in the Chemistry of Lanthanide-Doped Upconversion Nanocrystals. *Chem. Soc. Rev.* **38**, 976–98999 (2009).
7. Boyer, J. C. & van Veggel, Frank, C. J. M. Absolute Quantum Yield Measurements of Colloidal $NaYF_4$: Er^{3+}, Yb^{3+} Upconverting Nanoparticles. *Nanoscale* **2**, 1417 (2010).
8. Xu, W. *et al*. Ultra-broad Plasma Resonance Enhanced Multicolor Emissions in an Assembled Ag/$NaYF_4$:Yb,Er Nano-film. *Nanoscale* **4**, 6971–6973 (2012).
9. Li, A. H. & Lǔ, Q. Power-dependent Upconversion Luminescence Intensity in $NaYF_4$, Yb^{3+}, Er^{3+} Nanoparticles. *EPL.* **96**, 18001 (2011).
10. Mai, H. X., Zhang, Y. W., Sun, L. D. & Yan, C. H. Highly Efficient Multicolor Up-Conversion Emissions and Their Mechanisms of Monodisperse $NaYF_4$:Yb,Er Core and Core/Shell-Structured Nanocrystals. *J. Phys. Chem. C.* **111**, 13721–13729 (2007).
11. Bryan, M., Linda, A. & Andries, M. Lanthanide Ions As Spectral Converters for Solar Cells. *Phys. Chem. Chem. Phys.* **11**, 11081–11095 (2009).
12. Wang, J. W. & Peter, A. T. Upconversion for White Light Generation by a Single Compound. *J. Am. Chem. Soc.* **132**, 947–949 (2010).
13. Strek, W. *et al*. White Emission of Lithium Ytterbium Tetraphosphate Nanocrystals. *Opt. Express.* **19**, 14083–14092 (2011).
14. Wang, J. W., Hao, J. H. & Peter, A. T. Luminous and Tunable White-light Upconversion for YAG ($Yb_3Al_5O_{12}$) and $(Yb,Y)_2O_3$ Nanopowders. *Opt Lett.* **35**, 3922–3924 (2010).
15. Xu, S. *et al*. Observation of Ultrabroad Infrared Emission Bands in Er_2O_3, Pr_2O_3, Nd_2O_3, and Sm_2O_3 Polycrystals. *App. Phy. Exp.* **5**, 102701 (2012).
16. Yang, T. S. *et al*. Cubic sub-20 nm $NaLuF_4$-based Upconversion Nanophosphors for High-contrast Bioimaging in Different Animal Species. *Biomaterials* **33**, 3733–3742 (2012).
17. Yi, G. S. & Chow, G. M. Water-Soluble $NaYF_4$:Yb,Er(Tm)/$NaYF_4$/Polymer Core/Shell/Shell Nanoparticles with Significant Enhancement of Upconversion Fluorescence. *Chem. Mater.* **19**, 341 (2007).
18. Wang, F. *et al*. Tuning Upconversion Through Energy Migration in Core-Shell Nanoparticles. *Nat. Mater.* **10**, 968–973 (2011).
19. Schietinger, S., Aichele, T., Wang, H. Q., Nann, Thomas. & Benson, O. Plasmon-Enhanced Upconversion in Single $NaYF_4$:Yb^{3+}/Er^{3+} Codoped Nanocrystals. *Nano. Lett.* **10**, 134–138 (2010).
20. Liu, N., Qin,W. P., Qin, G. S., Jiang, T. & Zhao, D. Highly Plasmon-Enhanced Upconversion Emissions from Au@β-$NaYF_4$:Yb,Tm Hybrid Nanostructures. *Chem. Comm.* **47**, 7671–7673 (2011).
21. Zhang,W. H., Ding, F. & Chou, S. Y. Large Enhancement of Upconversion Luminescence of $NaYF_4$:Yb^{3+}/Er^{3+}Nanocrystal by 3D Plasmonic Nano-Antennas. *Adv. Mater.* **24**, OP236–OP241 (2012).
22. Saboktakin, M. *et al*. Metal-Enhanced Upconversion Luminescence Tunable through Metal Nanoparticle–Nanophosphor Separation. *ACS Nano.* **6**, 8758–8766 (2012).
23. Zhang, R. H. *et al*. Surface-Enhanced Fluorescence from Fluorophore-Assembled Monolayers by Using Ag@SiO_2 Nanoparticles *ChemPhysChem.* **12**, 992–998 (2011).
24. Rai, V. K. *et al*. Surface-plasmon-enhanced Frequency Upconversion in Pr^{3+} Doped Tellurium-oxide Glasses Containing Silver Nanoparticles. *J. Appl. Phys.* **103**, 093526 (2008).
25. Link, S., Mohamed, M. B. & El-Sayed, M. A. Simulation of the Optical Absorption Spectra of Gold Nanorods as a Function of Their Aspect Ratio and the Effect of the Medium Dielectric Constant. *J. Phys. Chem. B.* **103**, 3073–3077 (1999).
26. Zhu, Y. S. *et al*. Broad White Light and Infrared Emission Bands in YVO_4:Yb^{3+},Ln^{3+}(Ln^{3+} = Er^{3+}, Tm^{3+}, or Ho^{3+}). *Appl. Phy. Exp.* **5**, 092701–3 (2012).
27. Polosan, S., Bettinelli, M. & Tsuboi. T. Photoluminescence of Ho^{3+}:YVO_4 Crystals. *Phys. Status Solidi (C).* **4**, 1352-1355 (2007).
28. Saad, A. M., Mohamed, M. B., Abou Kana, M. T. H. & Azzouz, I. M. Synthesis Effect, Upconversion and Amplified Stimulated Emission of Luminescent CdTe NPs. *Optics & Laser Technology.* **46**, 1–5 (2013).
29. Zhao, J. B. *et al*. Single-nanocrystal Sensitivity Achieved by Enhanced Upconversion Luminescence. *Nature Nanotech.* **8**, 729–734 (2013).
30. Redmond, S., Rand, S. C., Ruan, X. L. & Kaviany, M. Multiple Scattering and Nonlinear Thermal Emission of Yb^{3+}, Er^{3+}:Y_2O_3 Nanopowders. *J. Appl. Phys.* **95**, 4069 (2004).
31. Subba Rao, G. V., Ramdas, S., Mehrotra, P. N. & Rao, C. N. R. Electrical Transport in Rare-earth Oxides. *J. Solid. State Chem.* **2**, 377–384 (1970).
32. Liu, Y., Wan, S. L. & Li, X. G. Visualizing High-temperature Spin Dynamics in $La_{1-x}Ca_xMnO_3$ from a Mapping of EPR Linewidth and g-factor. *J. Phys.:Condens. Matter.* **19**, 196213 (2007).
33. Wang, J. *et al*. Enhancing Multiphoton Upconversion Through Energy Clustering at Sublattice Level. *Nature Mater.* **13**, 157–162 (2014).
34. Liu, Y. S., Tu, D. T., Zhu, H. M. & Chen, X. Y. Lanthanide-doped Luminescent Nanoprobes: Controlled Synthesis, Optical Spectroscopy, and Bioapplications. *Chem. Soc. Rev.* **42**, 6924–6958 (2013).
35. Huang, P. *et al*. Lanthanide-Doped $LiLuF_4$ Upconversion Nanoprobes for the Detection of Disease Biomarkers. *Angew. Chem. Int. Ed.* **53**, 1252–1257 (2014).
36. Koch, S. W., Kira, M., Khitrova, G. & Gibbs, H. M. Semiconductor Excitons in New Light. *Nat. Mater.* **5**, 523–531 (2006).
37. Xiao, K. & Yang, Z. Blue Cooperative Luminescence In Yb^{3+}-Doped Barium Gallogermanate Glass Excited At 976 nm. *J. Fluoresc.* **16**, 755–759 (2006).

Acknowledgments

This work was supported by the Major State Basic Research Development Program of China (973 Program) (No. 2014CB643506), the National Natural Science Foundation of China (Grant No. 11374127, 11304118, 61204015, 81201738, 61177042, and 11174111), Program for Chang Jiang Scholars and Innovative Research Team in University (No. IRT13018).

Author contributions

W.X. conducted the most of investigation for the samples and wrote the main paper. H.W.S. supervised the project, had given valuable advices on the proceeding of this work, and revised the manuscript. X.L.M., X.C. and Y.S.Z. had provided precious suggestions on the selection of up-converison broad band phosphors. S.B.C. and L.T. supported the characterization of the samples. P.W.Z. and S.X. had provided precious suggestions on the photocurrent and EPR test. All authors discussed the results and commented on the manuscript at all stages.

Additional information

Supporting Information Available: The UCL spectra of Ag-SiO_2-Er_2O_3 composites under 808 nm excitation; UCL enhancement in Ag-SiO_2-Y_2O_3:Yb,Er nanocomposites; The power density dependence of photocurrent of Er_2O_3 NPs, Ag-SiO_2-Er_2O_3 composites on excitation power of 980 nm light.

Supplementary information accompanies this paper at http://www.nature.com/scientificreports

Competing financial interests: The authors declare no competing financial interests.

How to cite this article: Xu, W. *et al*. Ag-SiO_2-Er_2O_3 Nanocomposites: Highly Effective Upconversion Luminescence at High Power Excitation and High Temperature. *Sci. Rep.* **4**, 5087; DOI:10.1038/srep05087 (2014).